University of Groningen

Understanding the Impact of Bismuth Heterovalent Doping on the Structural and Photophysical Properties of CH3NH3PbBr3 Halide Perovskite Crystals with Near-IR Photoluminescence

Meng, Rui; Wu, Guangbao; Zhou, Jiyu; Zhou, Huiqiong; Fang, Honghua; Loi, Maria A.; Zhang, Yuan

IMPORTANT NOTE: You are advised to consult the publisher's version (publisher's PDF) if you wish to cite from it. Please check the document version below.

Document Version
Publisher's PDF, also known as Version of record

Link to publication in University of Groningen/UMCG research database

▌Semiconductors

Understanding the Impact of Bismuth Heterovalent Doping on the Structural and Photophysical Properties of CH₃NH₃PbBr₃ Halide Perovskite Crystals with Near-IR Photoluminescence

Rui Meng,[a, b] Guangbao Wu,[a] Jiyu Zhou,[a] Huiqiong Zhou,*[b] Honghua Fang,*[c] Maria A. Loi,[c] and Yuan Zhang*[a]

Abstract: A comprehensive study unveiling the impact of heterovalent doping with Bi³⁺ on the structural, semiconductive, and photoluminescent properties of a single crystal of lead halide perovskites ($CH_3NH_3PbBr_3$) is presented. As indicated by single-crystal XRD, a perfect cubic structure in Bi³⁺-doped $CH_3NH_3PbBr_3$ crystals is maintained in association with a slight lattice contraction. Time-resolved and power-dependent photoluminescence (PL) spectroscopy illustrates a progressively quenched PL of visible emission, alongside the appearance of a new PL signal in the near-infrared (NIR) regime, which is likely to be due to energy transfer to the Bi sites. These optical characteristics indicate the role of Bi³⁺ dopants as nonradiative recombination centers, which explains the observed transition from bimolecular recombination in pristine $CH_3NH_3PbBr_3$ to a dominant trap-assisted monomolecular recombination with Bi³⁺ doping. Electrically, it is found that the mobility in pristine perovskite crystals can be boosted with a low Bi³⁺ concentration, which may be related to a trap-filling mechanism. Aided by temperature (T)-dependent measurements, two temperature regimes are observed in association with different activation energies (E_a) for electrical conductivity. The reduction of E_a at lower T may be ascribed to suppression of ionic conduction induced by doping. The modified electrical properties and NIR emission with the control of Bi³⁺ concentration shed light on the opportunity to apply heterovalent doping of perovskite single crystals for NIR optoelectronic applications.

Introduction

Organic–inorganic hybrid perovskites, such as methylammonium lead halide MAPbX₃ (X = I, Br, Cl), are considered to be highly promising candidates for solution-processed semiconductor devices for energy conversion,[1–5] displays, and photo- or X-ray detector applications. In comparison to perovskite polycrystalline films, which are often accompanied by non-negligible levels of structural defects and molecular disorder,[6–11] single crystals of perovskite (PSC) are more advantageous with respect to fewer traps, longer exciton diffusion distances, superior photoluminescence (PL) properties, and enhanced stability.[6, 7] These merits render PSCs as an ideal testbed for fundamentally investigating the optoelectronic properties of this emerging class of materials.

Similar to traditional inorganic semiconductors, for example, silicon, it is highly desirable to achieve controllable doping for halide perovskites to attain the tunability of the electrical properties. So far, most adopted doping approaches for hybrid perovskites rely on the introduction of heterohalide atoms or organic anions with which the band gaps are tuned. These methodologies, despite effectiveness in certain aspects, cannot be considered for charge doping because of considerably changed band structures and the lack of controllability of the carrier density and resultant electrical conductivity (σ).

Recently, strategies based on heterovalent doping have been proposed to achieve modulations of electrical and optical behavior in halide perovskites.[12–18] It has been shown that the introduction of heterovalent Bi³⁺ into methyl bromide based perovskite (MAPbBr₃) precursor solutions could lead to charge doping of MAPbBr₃.[19–21] The success in Bi³⁺-based doping benefits from the ease of Bi³⁺ entering the octahedral cages because of the analogous electronic structures of Bi³⁺ with Pb²⁺ and an appropriate Goldschmidt tolerance factor (0.889).[20,22] As a result, the lattice structure in MAPbBr₃ hosts can be favorably maintained by partially substituted Pb²⁺ with

[a] R. Meng, G. Wu, J. Zhou, Prof. Y. Zhang
School of Chemistry, Beijing Advanced Innovation Center
for Biomedical Engineering, Beihang University
No. 37 Xueyuan Road, Beijing 100191 (P.R. China)
E-mail: yuanzhang@buaa.edu.cn

[b] R. Meng, Prof. H. Zhou
CAS Key Laboratory of Nanosystem and Hierarchical Fabrication
CAS Center for Excellence in Nanoscience National Center
for Nanoscience and Technology, Beijing 100190 (P.R. China)
E-mail: zhouhq@nanoctr.cn

[c] Dr. H. Fang, Prof. M. A. Loi
Zernike Institute for Advanced Materials, University of Groningen
Nijenborgh 4, 9747 AG Groningen (The Netherlands)
E-mail: honghua.fang@gmail.com

Supporting information and the ORCID identification number(s) for the author(s) of this article can be found under:
https://doi.org/10.1002/chem.201805370.

Bi^{3+}. However, the necessity of Bi^{3+} doping has been challenged by the recent finding by Snaith et al.[19] that the introduced heterovalent Bi^{3+} dopants may result in the formation of impurity states in the perovskite crystal, which can serve as a nonradiative recombination center.[19,23] As a result, the PL lifetime and carrier diffusion length are impaired. In addition, the impact of Bi^{3+} doping on the favored photon recycling effect (PRE) has been investigated by Yamada et al.[21] It was found that the power conversion efficiency became considerably weakened after Bi^{3+} doping, due to the shortened PL lifetime. Despite these arguments on the negative effects of the optical properties of perovskites, the photophysical origin of doping-induced charge trapping is still poorly understood. In addition, how the presence of Bi^{3+} dopants affects the electronic characteristics in CH$_3$NH$_3$PbBr$_3$ is, as yet, unclear. Obtaining enriched insights into Bi doping will be beneficial for achieving meaningful applications of heterovalent doping for perovskite-based optoelectronic devices.

Herein, based on high-quality and millimeter-sized single crystals of bismuth-doped perovskite MA(Pb$_{1-x}$Bi$_x$Br$_3$) attained by means of facile solution growth, we present a comprehensive picture for the impact of Bi doping on the structural, semiconducting, and PL properties of MAPbBr$_3$-based PSCs. Aided by single-crystal XRD (SC-XRD), we resolved the lattice structure of Bi^{3+}-doped PSCs, which showed a slightly reduced volume (208.38 Å^3) of the cubic crystal, with a Bi^{3+} concentration of 10%. It is shown that the carrier mobility in MAPbBr$_3$ PSCs with slight doping of Bi^{3+} becomes considerably higher; this can be related to trap filling of dopant-induced mobile carriers. This process is confirmed by means of power-dependent time-resolved PL spectroscopy. Based on temperature (T)-dependent electrical measurements, we assessed the activation energy (E_a) of the electrical conductivity (σ) in Bi-doped crystals. A transition from a larger E_a in the high-T regime to smaller E_a in the low-T regime was found, which closely correlated the cubic to tetragonal phase transition occurring in MA(Pb$_{1-x}$Bi$_x$)Br$_3$ PSCs. The increase of E_a in the higher T regime may be partially ascribed to coexisting ionic conduction in the crystals. Alongside the significantly quenched PL in the visible region with increased Bi/Pb ratio, a new PL appears in the near-infrared (NIR) regime ($\approx$1080 nm) after Bi^{3+} doping; thus indicating radiative charge recombination originating from Bi^{3+} ions. We observe blueshifts of visible emission in steady-state PL with increasing Bi/Pb ratio, which is likely to result from self-quenching effects occurring at the surface of MA(Pb$_{1-x}$Bi$_x$)Br$_3$, and thus, reduces the self-absorption effect. The combination of these results indicates that, with a well-controlled doping level of Bi^{3+}, amelioration of the electrical properties can be realized for PSCs. Also, the NIR emission upon Bi doping suggests the possibility of applying heterovalent doping of MAPbBr$_3$ single crystals for NIR optoelectronic applications.

Results and Discussion

Pristine and Bi^{3+}-doped MAPbBr$_3$ (CH$_3$NH$_3$PbBr$_3$) single crystals were attained by using the inverse temperature crystallization

(ITC) method reported elsewhere;[20,24–26] the growth procedures are schematically illustrated in Figure 1a. To start, the precursor solution was prepared by mixing bromomethylamine with bismuth tribromide at selected Pb/Bi ratios to form a supersaturated solution at 90 °C. Single crystals of MA(Pb$_{1-x}$Bi$_x$)Br$_3$ were gradually precipitated from the precursor solution due to the poor solubility of organic–inorganic hybrid halide perovskite in specific organic solvents. MA(Pb$_{1-x}$Bi$_x$)Br$_3$ PSCs of 4–5 mm in diameter were attained within 2 days. As shown by the pictures in Figure 1b, the color of Bi^{3+}-doped crystals darkens with increasing Bi^{3+} concentration in the feed solution. This tendency indicates a variation in the absorption, and possibly band gap, after doping.

To understand the structural properties of MA(Pb$_{1-x}$Bi$_x$)Br$_3$, we performed SC-XRD measurements with various concentrations of Bi^{3+} and the resolved lattice structures are comparatively shown in Figure 1c. The complete crystal structures of pristine and 10% Bi^{3+}-doped MAPbBr$_3$ are displayed in Figure S1 in the Supporting Information. Through analyzing the crystal data, the pure MAPbBr$_3$ unit cell exhibits a cubic structure ($Pm3m$ (221) space group) with $a=b=c=5.9380$ nm, leading to a cell volume of 209.373 Å^3. By comparing the unit cell parameters of MA(Pb$_{0.9}$Bi$_{0.1}$)Br$_3$ with those of cubic MAPbBr$_3$, a contraction in the cell was found. For example, at 10% doping, the cell volume reduces to 208.38 Å^3, with $a=b=c=5.9286$ nm. A similar tendency in cell contraction was observed in MA(Pb$_{1-x}$Bi$_x$)Br$_3$ with different doping concentrations (see Table S1 in the Supporting Information). However, it is noteworthy that the difference between the lattice constants of Pb and Bi should be 1.6 pm,[51] but much larger changes were identified in our case with Bi^{3+} doping, for example, a reduction in a (or b or c) by 9.4 pm was identified. The result seems to suggest the formation of complexed defect states after Bi^{3+} doping. Regardless of the doping concentration, the lattice in the Bi-doped crystals remains cubic, which agrees with the prediction in terms of the tolerance factor. For confirmation, we further calculated SC-XRD patterns (see results in Figure 1d). The attained XRD peaks are in good agreement with those of powder XRD (see Figure 1e) experimentally attained on the same set of samples. In powder XRD, we note a shift toward higher angles for 002 peaks, which is in line with the observed cell contraction after doping. This phenomenon can be ascribed to the incorporation of smaller Bi^{3+}, with ionic radius of 103 pm, with respect to bulkier Pb^{2+} (radius = 119 pm). As a result, the volume of the octahedral cage in the unit cell becomes reduced.

The presence of Bi is examined by means of XPS analysis of pristine MAPbBr$_3$ and 10% Bi^{3+}-doped MAPbBr$_3$ crystals. As shown in Figure 1f, the doublet XPS peaks positioned at 159.1 and 164.4 eV are assigned to Bi. This result confirms the presence of Bi in solid perovskite crystals. As observed from high-resolution XPS spectra of core-level atoms (Figure S2 in the Supporting Information), the Bi 4f doublet peaks appear at 159.1 (Bi 4f$_{7/2}$) and 164.4 eV (Bi 4f$_{5/2}$). These BEs are 0.3 eV smaller than the values reported for Bi^{3+} ions;[27] this may be ascribed to different chemical environments. We attempted to understand the chemical bonding of Bi—Br in terms of BE. To
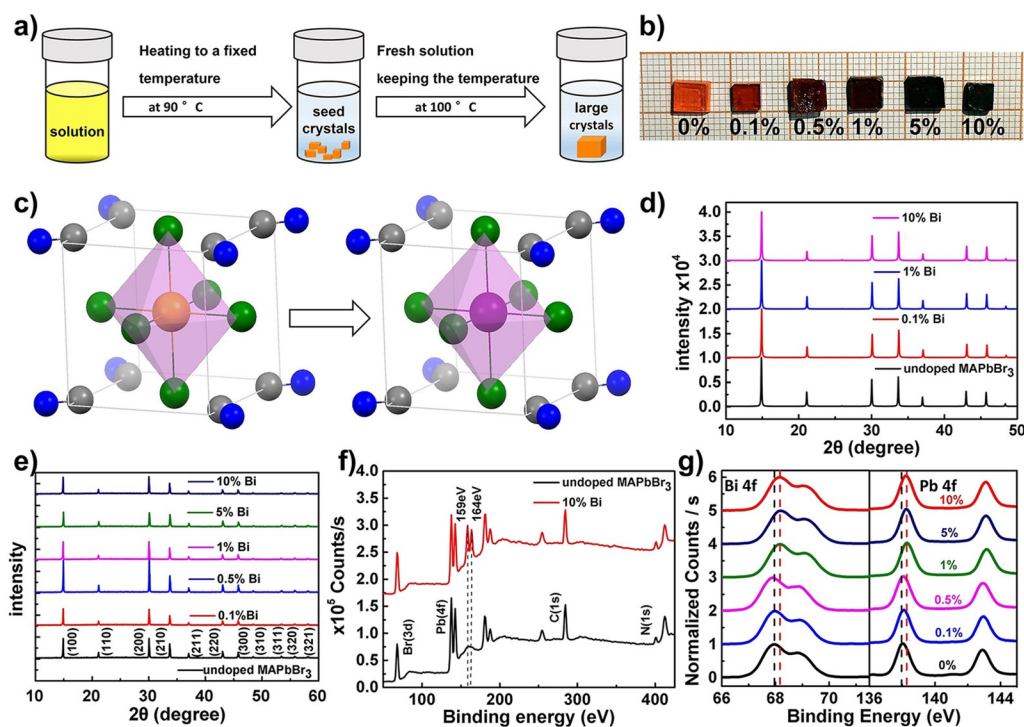
Figure 1. a) Schematic illustration of the crystallization of MA(Pb$_{1-x}$Bi$_x$)Br$_3$ by using an ITC method. b) Pictures of bismuth-doped halide PSCs (MA(Pb$_{1-x}$Bi$_x$)Br$_3$) with various Pb/Bi ratios. From left to right: $x=0$–0.1. c) Crystal structures of pure MAPbBr$_3$ and MAPbBr$_3$ with 10% Bi^{3+} (gray: carbon; blue: nitrogen; green: bromine; orange: lead; purple: bismuth) resolved by SC-XRD. d) Calculated SC-XRD patterns of pristine and Bi-doped MAPbBr$_3$. e) Powder XRD patterns of pristine and Bi-doped MAPbBr$_3$ crystals. f) X-ray photoelectron spectroscopy (XPS) survey spectra of pure MAPbBr$_3$ and Bi^{3+}-doped MAPbBr$_3$ (10%). g) High-resolution XPS core-level Bi 4 f and Pb 4 f spectra of MAPbBr$_3$ with different Bi^{3+} concentrations. Dashed black (for pristine) and red (for 10% doping) lines indicate the shift in binding energies (BEs) of Bi 4 f and Pb 4 f with varied Bi^{3+} concentrations.

facilitate our comparison, all XPS spectra were calibrated by the reference C 1 s peak at 284.8 eV. From the results shown in Figure 1 g, we note evident shifts in the BEs of Pb 4 f and Bi 4 f doublets toward high energy after Bi^{3+} doping. The shift in BE is in accordance with the concentration of Bi^{3+}, that is, the largest BE was found in the crystal with the highest doping (MA(Pb$_{0.9}$Bi$_{0.1}$)Br$_3$). This behavior can be interpreted by the weaker electronegativity of Bi (2.02) with respect to that of Pb (2.33). Similar effects have been observed in the XPS spectra of MAPb$_{1-x}$Sb$_{2x/3}$V$_{x/3}$I$_3$ upon partial Sb substitution.[28]

Figure 2 a shows UV/Vis/NIR spectra of MA(Pb$_{1-x}$Bi$_x$)Br$_3$ ($x=$ 0–0.1) with different Bi/Pb ratios. In accordance with previous studies,[14, 20, 29, 30] the absorption cutoff displays a progressive redshift with increasing concentration of Bi^{3+}. At the highest doping ratio (10%), the cutoff ends at $\lambda \approx 680$ nm, which is shifted by about 100 nm with respect to the pristine crystal with a cutoff at $\lambda \approx 580$ nm. With the systematic change of absorption cutoffs, the absorption of MA(Pb$_{1-x}$Bi$_x$)Br$_3$ ($x=0$–0.1) nearly covers the whole visible spectrum. In addition to the redshifts, we note the broadened absorption in the tail regions after Bi^{3+} doping (1–10%). These features could originate from the absorption of impurity states induced by Bi in the heavily doped crystals.[31] In Figure 2 b, we plot the shift of absorption cutoffs with respect to the pristine crystal. The saturated shift in absorption at higher doping concentrations agrees with the trend observed previously.[20] The narrowing of the band gap in Bi^{3+}-doped perovskites was postulated to arise from the in-

teraction of electrons with positive impurities, causing variations in the density of states (DOS).[32] This was confirmed by a recent study by Snaith et al.,[19] who showed that the redshifted absorption (with deepened colors) was merely caused by the increased DOS for the sub-band gap related to defects in the doped crystals and the band gap was not changed by Bi^{3+} doping.

To better understand the optical properties impacted on by the presence of Bi^{3+} dopants, we examined the PL properties of MA(Pb$_{1-x}$Bi$_x$)Br$_3$ PSCs (Figure 2 c). Interestingly, we observe two emission bands from the doped crystals: one is located in the visible region and the second in the NIR region. In comparison with pristine crystals, doped crystals are found with a clear blueshift in the visible PL spectrum with the maximal shift of 15.37 nm, which is in stark contrast to the absorption. If the band gap becomes narrowed after doping, one expects analogous trends of PL, given the small Stokes shift in perovskites.[33] The PL shift is in the opposite direction to that of the absorption cutoff, which means that the latter should not originate from a reduced gap, but other contributions. By taking the argument that the PL from the tail/impurity states in the doped perovskite is likely to be nonradiative, the results indicate that the band gap is not narrowed with increased Bi doping levels. Regarding the blueshifts in the PL, this effect could be attributed to self-quenching of the PL on the surface of crystals due to the decreased exciton diffusion length and photon cycling after doping.[34] We further compared the PL in-
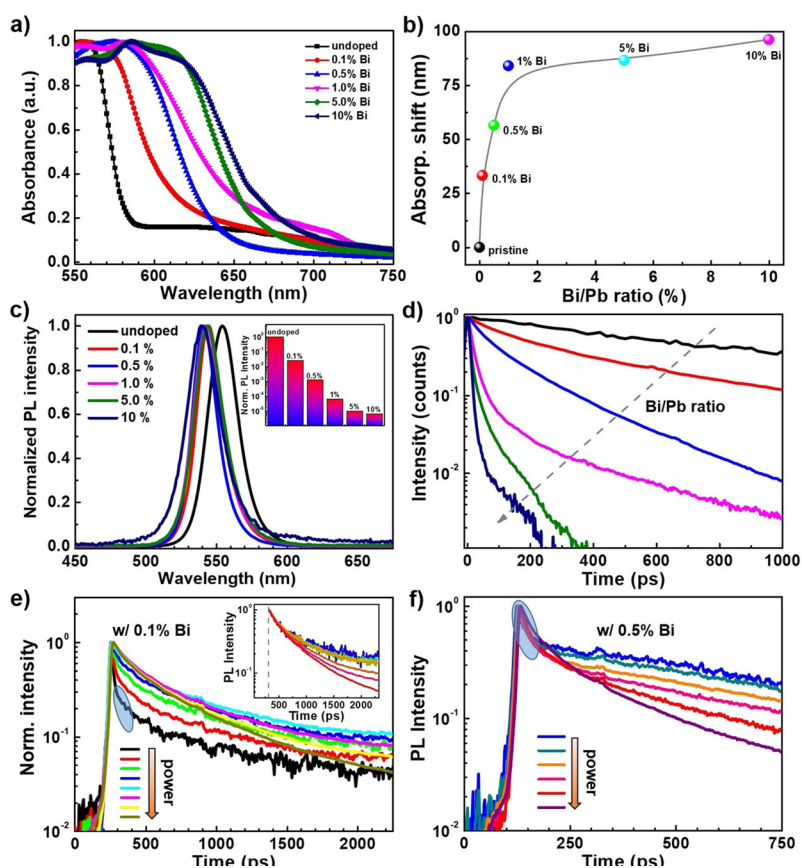
Figure 2. a) Normalized UV/Vis/NIR absorption spectra of pristine and Bi-doped MAPbBr$_3$ crystals at different concentrations. b) Shift of absorption cutoffs as a function of Bi concentration with respect to pristine MAPbBr$_3$. c) Normalized steady-state PL spectroscopy of single crystals of MA(Pb$_{1-x}$Bi$_x$)Br$_3$ ($x=0$–0.1). Inset: A comparison of absolute PL intensity of various MA(Pb$_{1-x}$Bi$_x$)Br$_3$ crystals. d) Time-resolved PL spectroscopy of MAPbBr$_3$ crystals with various Bi concentrations. e) PL decay traces at different laser powers of MAPbBr$_3$ crystals with 0.1% Bi doping. Inset: Decay traces of time-resolved PL in different MA(Pb$_{1-x}$Bi$_x$)Br$_3$ crystals normalized at the PL intensity at 310 ps, without showing the ultrafast decay part. f) PL decay traces at different excitation laser powers for MAPbBr$_3$ crystals with 0.5% Bi.

tensity of MA(Pb$_{1-x}$Bi$_x$)Br$_3$ PSCs (Figure 2c, inset). The substantially reduced PL intensity (up to 5 orders of magnitude) indicates that the defect states induced by Bi doping can serve as a recombination center upon which charges recombine nonradiatively. As shown in Figure 2d, the reduced steady-state PL is in association with decrease in PL lifetimes. The PL lifetime of the monodecay, which dominates the behavior in the pristine crystal, changes to biexponential decay as x increases from 0 to 0.1. Generally, the decay at longer timescales is related to PL in the bulk region of crystals and with increasing Bi concentration; faster decay in this temporal regime may be connected to charge trapping/detrapping processes with increased defect states. This observation is in agreement with the disappearance of photon-cycling effects after Bi doping, which has been explained by a shortened exciton diffusion distance.[35]

More in-depth understanding of the role of Bi doping is achieved through power-dependent PL decay kinetics (Figure 2e). Taking the example of a dilute doping (0.1%), we observe an ultrafast decay process in the first 250 ps under a low excitation power. This behavior could be understood by ultrafast localization of photocarriers into the carrier-trapping centers. Such "abnormal" rapid decay disappears with increasing excitation power, which suggests saturation of the filled defect

density. Interestingly, the lifetime of the slow-decay component is almost independent of the excitation fluence at low-power excitation. However, the PL kinetics obtain bimolecular recombination behavior at elevated power. To better understand this interesting observation, the PL decay traces at different laser powers were normalized to the intensities at 310 ps, which was long enough to end the rapid decay. As observed in the inset of Figure 2e, regular decay behavior is observed, with the PL becoming longer lived at lower excitations, due to reduced bimolecular recombination. These results highlight the trap-filling process with photoinduced carriers in the lightly doped MAPbBr$_3$ crystals. With filling of the traps by light-induced carriers, bimolecular recombination becomes dominant. For comparison, we examined power-dependent PL decays in the 0.5% doped crystal, which presumably contained a higher level of traps (see Figure 2f). In contrast to the results in Figure 2e, the ultrafast decay does not vanish with increasing laser power in the early stages. This phenomenon is interpreted by increased defect states at higher doping levels, such that trap filling cannot entirely eliminate the Shockley–Read–Hall (SRH) process. We further explored the recombination order in crystals by plotting the intensity of PL against laser power. In the absence of traps, the dominant bimolecular re-

combination should yield a low power dependence ($\approx P^\alpha$), in which $\alpha = 2$, whereas, in the dominating SRH process, the resultant monomolecular recombination can result in $\alpha = 1$. To enable precise analysis, herein we took the values of PL intensity at decay time = 0 from the decay kinetics. As such, the result should reflect more realistically the recombination properties in crystals and exclude the photon-cycling effect. Based on the fittings shown in Figure S3 in the Supporting Information, the pure crystal is associated with $\alpha = 2.02$, which agrees with the bimolecular process involving mobile (free) carriers. With increasing Bi doping concentration, the power monotonously decreases, for example, it reduces to 1.55 with 0.1% Bi doping and further to 1.27 with 0.5% Bi. From the reduction of recombination order, there is evidence that bimolecular recombination in the pristine MAPbPbBr$_3$ transits to a mixture of bi- and monomolecular recombination with low doping and becomes dominated by the monomolecular process at higher Bi doping levels due to increased defect densities.

To further understand the impact of Bi doping electrically, next we measured the electrical conductance. Figure 3a (inset) illustrates the device structure utilized, in which MA(Pb$_{1-x}$Bi$_x$)Br$_3$ PCSs were sandwiched between the two Ag contacts. A thin layer comprising of liquid Ga was applied atop the thermally deposited Ag contact to increase the contact property, which was found to be essential for our low-temperature measurements. In such a device configuration, the orientation of conductivity (or σ) is normal to the largest natural crystal facade (100 plane). We purposely applied low biases up to 20 V; the maximal electrical field was 1×10^4 V m^{-1} (crystal thickness of ≈ 2 mm) to mitigate the electrical poling effect.[36,37] Figure 3a displays current versus bias (IV) characteristics measured on

MA(Pb$_{1-x}$Bi$_x$)Br$_3$ PSCs with various Bi concentrations. The dark current in the pristine crystal ranges in nA; this indicates an intrinsically low σ and high purity of the MAPbBr$_3$ PSC. The current progressively increases upon increasing x from 0 to 0.1, as a result of enhanced σ.[38] The increase in current becomes saturated if the doping level is further increased, for example, from 1 to 10% Bi^{3+}. Based on the IV curves, the conductivity was determined according to Ohm's law. As shown in Figure 3b, σ of MAPbBr$_3$ starts at 6.3×10^{-7} Ω^{-1} m^{-1} without doping and sharply increases to 1.36×10^{-3} Ω^{-1} m^{-1} at 1.0% Bi and saturates at 10% with σ up to 4.83×10^{-3} Ω^{-1} m^{-1}. The value of σ in MAPbBr$_3$ can be tuned by nearly four orders of magnitude through Bi^{3+} doping, and the saturation trend fully agrees with previous observations on the same system.[20,39] Given the importance of charge carrier mobility (μ), which plays a critical role in ultimate device behavior, in perovskites, we attempted to assess μ in MA(Pb$_{1-x}$Bi$_x$)Br$_3$ with variation of x. A direct probe of μ along the direction perpendicular to the (100) plane can be challenging with current techniques. Based on Equation (1), in which n_d is the carrier concentration and q is the elementary charge, μ can be determined if n_d and σ are known.

$$\sigma = n_d q \mu \tag{1}$$

For this purpose, we estimated the carrier density induced by Bi doping through impedance analysis. Based the well-established Mott–Schottky relationship, $d(C^{-2})/d(V) = 2/(qA^2\varepsilon n_d)$ (C is capacitance, A is the effective device area, ε is the dielectric constant of perovskites), the values of n_d were extracted. Figure 3c displays the determined n_d values as a function of Bi/Pb
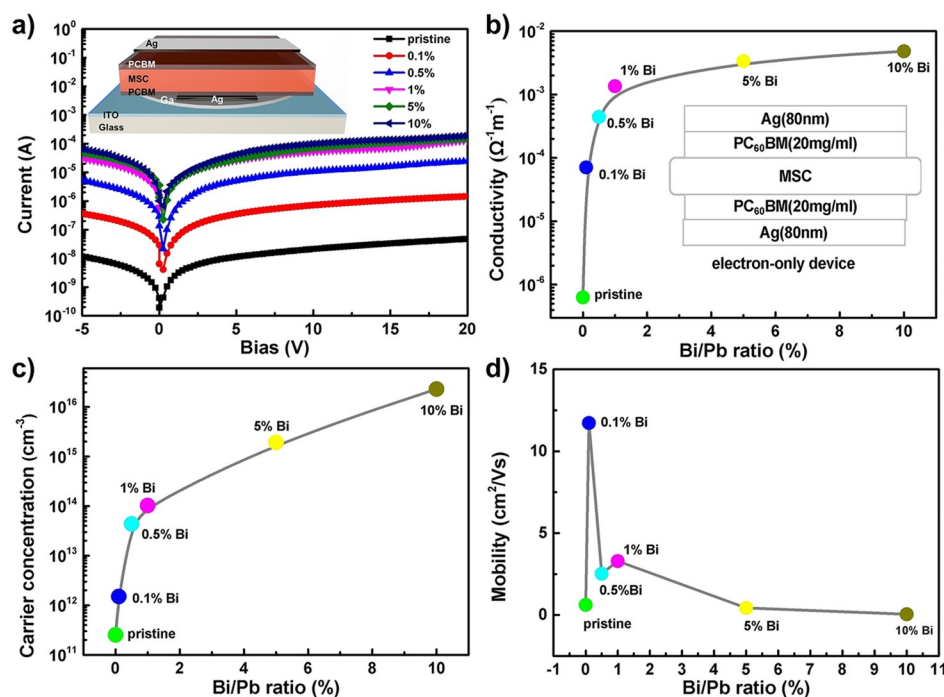

Figure 3. a) Current versus voltage (IV) characteristics of MA(Pb$_{1-x}$Bi$_x$)Br$_3$ ($x = 0$–0.1) single-crystal-based electron-only devices. Inset: Schematic structure of electron-only devices. b) Conductivity, c) carrier concentration, and d) mobility of MA(Pb$_{1-x}$Bi$_x$)Br$_3$ ($x = 0$–0.1) single crystals as a function of Bi/Pb ratio. ITO = indium tin oxide, PC$_{60}$BM = [6,6]-phenyl C$_{61}$-butyric acid methyl ester, MSC = MA(Pb$_{1-x}$Bi$_x$)Br$_3$ single crystal.

ratio. The intrinsic background carrier density falls in the order of 10^{11} cm^{-3}, which is seemingly slightly higher than that of the value reported in the literature, possibly due to variations in the crystals. The value of n_d increases by nearly 3 orders at 1.0% Bi, reaching 2×10^{14} cm^{-3} and is further boosted to about 10^{16} cm^{-3} upon heavy doping (10%). A nonlinear increase of n_d with Bi/Pb concentration is noted and the enhancement of n_d tends to become saturated at higher Bi doping levels. This tendency may indicate that, with increasing doping level, the portion of B^{3+} dopants added that are eventually incorporated into MAPbBr$_3$ crystals is likely to reduce. This is consistent with the relative peak percentage of Bi measured by means of XPS (see Table S3 in the Supporting Information).

Based on the determined n_d and σ values, the mobility was calculated according to Equation (1) and the results are shown in Figure 3d. The mobility is 0.62 cm^{2}Vs^{-1} in the pristine crystal and it sharply increases to 11.72 cm^{2}Vs^{-1} with a Bi concentration of 0.1%. Upon further increase the doping level, the mobility abruptly decreases and approaches the level of the pristine crystal (with 5 and 10% Bi). This trend was affirmed by devices containing hole-transporting (electron-blocking) interlayers based on N2,N2,N2′,N2′,N7,N7,N7′,N7′-octakis(4-methoxyphenyl)-9,9′-spirobi[9H-fluorene]-2,2′,7,7′-tetramine (Spiro-OMeTAD; see Figure S4 in the Supporting Information). Consistently, we observe the tendency for the evolution of mobility with doping (Figure S4d in the Supporting Information). The enlargement of μ at low Bi concentrations is likely to be ascribed to the filling of traps (e.g., in the surface area of nonpassivated crystals) by doping-induced mobile carriers. Further increases in Bi concentration tend to raise the DOS for defects, which are harmful for charge transport due to impurity scattering.[40] Our results indicate the significance of controlling the doping level to attain improved electrical properties.

To gain knowledge of the thermal E_a of σ, we measured σ in PSCs at different T. Concerning the nature of electron doping with Bi, a thin PC$_{60}$BM electron-transporting layer was inserted into the devices (see device architecture in Figure 3a, inset), which was found to be necessary to yield reliable T dependencies. Figure S5 in the Supporting Information shows dark IV characteristics of MA(Pb$_{1-x}$Bi$_x$)Br$_3$ (with x ranging from 0 to 0.001) at different T. In all devices, the current decreases with decreasing T, which results in a positive T coefficient. Moreover, we observe a moderate hysteresis in the IV curves that increas-

es with the reduction of T. The origin of hysteresis in perovskites has been ascribed to multiple factors, including traps and ion motion.[41–44] Because the ionic conductance should be attenuated at lower T, the more severe hysteresis might be ascribed to enhanced charge trapping at lower T, which was previously observed in MAPbI$_3$ perovskites.[45] Figure 4a shows the determined values of σ as a function of T for PSCs with different Bi/Pb ratios. We note two distinct T dependencies at 250–350 and 225–150 K, resulting in stronger and weaker E_a in the high- and low-T regimes, respectively. In MAPbBr$_3$ perovskites, the cubic to tetragonal phase transition is likely to occur at about 237 K.[46] The transition of E_a closely correlates with the phase transition, which indicates the influence of structural variation on the thermal activation of σ. As shown in a previous study on field-effect mobilities in perovskites, the T coefficient of mobility was ascribed to the MA$^+$ dipole disorder. In Figure 4a, the larger E_a in the high-T regime seems to be in line with the enlargement of MA$^+$ cations. Based on the linear fit, by assuming an Arrhenius T dependence for σ, E_a was determined for the crystals doped with different Bi concentrations. As shown in Figure 4b, in the high-T regime, we extracted $E_a=68.9$ meV without doping; this increased with Bi/Pb ratios, peaking at 322.5 meV with 0.5% Bi (meV) and decreasing to 221.9 meV with 1.0% Bi. A similar trend was observed in the low-T region, corresponding to the dominant tetragonal lattice structure. Overall, reduced E_a in the low-T region is in line with decreased ionic conduction in perovskites. The dependence of E_a on the doping level may be reconciled by the interplay between enlarged E_a for ionic conduction induced by Bi and reduced E_a for electrical conduction. The former is expected to reduce with a larger σ. Previous studies on doping also highlight the possibility to observe enlarged E_a for σ in the heavy doping regime, which is related to broadening of the DOS for the conduction bands.[47] This effect generally occurs with $n_d>10^{18}$ cm^{-3}, which seems to be out of the range achieved by our Bi doping. Another contribution to the activation of electrical conductance comes from charge trapping. Currently, E_a arising from trapping/detrapping cannot be decoupled from the results in Figure 4b, although it appears to be insignificant concerning the dominant shallow traps in perovskites with a low formation energy for defects.[48]

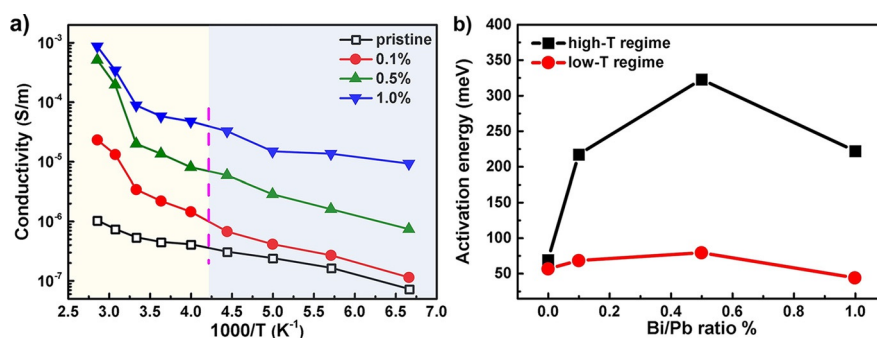Heterovalent doping with Bi was argued to primarily serve as a nonradiative recombination center that impaired the PL

Figure 4. a) Temperature dependence of conductivity in pure and Bi-doped MAPbBr$_3$ single crystals. b) E_a in MA(Pb$_{1-x}$Bi$_x$)Br$_3$ ($x=0$–0.01) with different Bi^{3+} concentrations determined at high- (with the background in light yellow) and low-T (with the background in light blue) regimes.
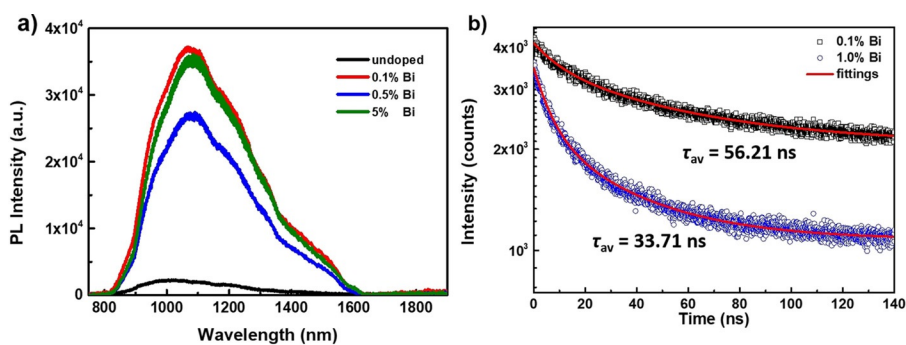
Figure 5. a) NIR PL of MA(Pb$_x$Bi$_{1-x}$)Br$_3$ single crystals. b) Time-resolved PL of Bi-doped crystals probed in the NIR region alongside exponential fittings. Also included are the averaged decay times (τ_{av}) for PL in the NIR regime.

properties in MAPbBr$_3$.[49] However, we found that the presence of Bi^{3+} dopants could lead to an enhanced optical response of MAPbBr$_3$ in the NIR regime. As shown in Figure 5a, in contrast to the rather weak and broad PL signal in pristine MAPbBr$_3$ crystals (with the peak positioned at around 1000 nm), new PL peaks at about 1080 nm were observed after Bi doping. The peak intensity and position barely varied with Bi concentration and the spectral shape resembled that of Bi^{3+}-doped samples, but considerably differed from that of the undoped crystal. These new PL features may be assigned to the emission of the in-band states induced by the Bi^{3+} dopants.[50] Regarding the photophysical origin, it is possible that energy transfers from the PL of MAPbBr$_3$ to the radiative states in the NIR regime. We also note that the incremental variation of the Bi/Pb ratio does not lead to a progressive change in the PL intensity in the NIR regime. This result may be related to an inhomogeneous distribution of Bi^{3+} dopants. The exact origin of the PL emission in the presence of Bi^{3+} doping will require further investigation for full elaboration. We also assessed the PL lifetime at about 1020 nm and the decay kinetics (Figure 5b). With a biexponential decay model, the time constants corresponding to faster and slower decays were extracted (Table S2 in the Supporting Information). The averaged PL lifetimes (τ_{av}), according to Equation (2), are 56.21 and 33.71 ns for 0.1 and 1.0% doped crystals, respectively.

$$\tau_{av} = \frac{A_1\tau_1^2 + A_2\tau_2^2}{A_1\tau_1 + A_2\tau_2} \qquad (2)$$

The decay of the NIR emission in the pristine crystal cannot be measured, due to weak PL intensity. The decay time seems to be irrelevant to the Bi doping level and is relatively long, in the region of 12 ns. Further investigations are required to fully explain this observation. The results in Figure 5 (and Figure S7 in the Supporting Information) suggest an opportunity for applying Bi doping for perovskite-based optoelectronic applications in the NIR regime.

Conclusions

We comprehensively investigated the structural, photophysical, and electrical properties of single crystals of MAPbBr$_3$ perovskites with Bi^{3+}-based heterovalent doping. SC-XRD indicated

that incorporating Bi^{3+} into MAPbBr$_3$ maintained the stable cubic lattice structure, with a slight contraction due to the smaller radius of Bi^{3+}. Steady-state and time-resolved PL spectroscopic measurements, in conjunction with electrical analysis, unraveled the role of Bi doping: at low concentrations, doping tended to result in trap filling, while trap centers could be formed with increased Bi/Pb ratios, resulting in a transition from bimolecular recombination in the pristine crystal to trap-assisted monomolecular recombination after doping. The slight blueshifts in steady-state PL with doping are likely to be ascribed to PL self-quenching on the surface of MA(Pb$_{1-x}$Bi$_x$)Br$_3$ crystals. This result ruled out the narrowing of band gaps that was intuitively deduced from the redshift in absorption cutoffs in Bi-doped crystals. We achieved an enhanced mobility in MAPbBr$_3$ by 19-fold with low doping (0.1%) and the mobility adversely decreased to the level of the pristine crystal with 5 and 10% Bi. Based on T-dependent conductivity measurements, we identified two distinct E_a values in the high- and low-T regimes, with the transition closely correlated to the cubic to tetragonal phase transition occurring at around 240 K. In the high-T regime (250–350 K), E_a displays a nonmonotonous change with doping level and peaks with 0.5% Bi. Such behavior may be reconciled by the interplay between enlarged E_a for ionic conduction induced by Bi and reduced E_a for electrical conduction. We also observed a pronouncedly increased PL in the NIR region in MAPb$_{1-x}$Bi$_x$Br$_3$ crystals, but the exact photophysical origins are yet to be clarified and require future study. Our results help to clarify the fundamental role of heterovalent doping with Bi and highlight the importance of controlling the doping level in the low-doping regime to render positive optoelectronic effects. From a broader perspective, future efforts may be dedicated to seeking alternative metal-ion doping with considerably reduced defects states; this could benefit meaningful applications of heterovalent doping for perovskite optoelectronic devices.

Experimental Section

Materials

Lead bromide ($\geq$99.999%) was purchased from Lumtec. DMF (3A dry, $\geq$99.8%) and bismuth bromide ($\geq$98%) were purchased from Sigma–Aldrich. MABr ($\geq$99%) was purchased from Dyesol Ltd (Aus-

tralia). All salts and solvents were used as received without any further purification.

Synthesis of MA(Pb$_{1-x}$Bi$_x$)Br$_3$ single crystals

A 1 M solution containing PbBr$_2$ and MABr or BiBr$_3$ was prepared in DMF. Both solutions were prepared at room temperature. The two solutions in DMF were mixed in a vial that was kept in an oven undisturbed at 90 °C. Small seed crystals could be readily harvested through this method. The seeds were placed into fresh solution and heated at about 100 °C for 6 h and, within 2 days, large crystals with diameters between 4 and 5 mm were attained. The doping concentration of Bi was controlled by the ratio of Bi/Pb in the precursor solutions.

MA(Pb$_x$Bi$_{1-x}$)Br$_3$ single-carrier device fabrication

Initially, PC$_{61}$BM was presolubilized in chlorobenzene (CB) at a concentration of 20 mg mL^{-1}. The PC$_{60}$BM/CB solution was drop-cast atop the two surfaces of MAPb$_x$Bi$_{1-x}$Br$_3$ crystals. Then 60 nm Ag electrodes were thermally evaporated on the PC$_{60}$BM layers. For bottom contacts, PSCs with PC$_{60}$BM/Ag were transferred onto precleaned ITO substrates with application of metallic molten Ga. Before testing, the substrates were cooled below 20 °C to solidify Ga. For hole-only devices, Spiro-OMeTAD hole-transporting (electron-blocking) interlayers were deposited atop the surfaces of MA(Pb$_x$Bi$_{1-x}$)Br$_3$ crystals by spin-coating. Finally, the 80 nm Au contact was thermally evaporated on top of Spiro-OMeTAD interlayers.

Temperature-dependent I–V measurements

Current versus voltage characteristics were measured by using a Keithley 4200-SCS semiconductor parameter analyzer. For temperature-dependent conductivity measurements, the samples were cooled by liquid nitrogen in a Lakeshore vacuum probe station, and the temperature was controlled by a LakeShore temperature controller.

Characterization

Powder XRD patterns (room temperature) were recorded on a Rigaku D/MAX-TTRIII (CBO) diffractometer with Cu$_{K\alpha}$ radiation ($l =$ 1.542 Å) operated at 40 kV and 200 mA. SC-XRD data collection was carried out on a Rigaku AFC-10/Saturn 724+CCD diffractometer with graphite-monochromated Mo$_{K\alpha}$ radiation ($\lambda = 0.71073$ Å) by using the multiscan technique. The structures were determined by direct methods with SHELXS-971 and refined by full-matrix least-squares procedures on F^2 with SHELXL-97.2. All non-hydrogen atoms were obtained from difference Fourier map and subjected to anisotropic refinement by full-matrix least squares on F^2. Hydrogen atoms were obtained geometrically and treated as riding on the parent atoms or were constrained in specific locations during refinements. UV/Vis/NIR diffuse reflectance spectra were measured at room temperature by using a UV/Vis/NIR spectrophotometer (UV-3600) with an integrating sphere attachment operating in the 300–1600 nm region. PL measurements were performed at room temperature under excitation at $\lambda = 400$ nm by a mode-locked Ti-Sapphire laser (Mira 900, Coherent). A Hamamatsu charge-coupled device (CCD) camera was used to record the visible PL spectra, and an Andor 1.7 μm InGaAs camera was used to measure the emission spectra in the NIR region. The spectral response of the instrument was calibrated by using a calibration light source. Time-resolved PL measurements were performed by using a Hamamatsu Streak camera operated in synchroscan mode. Nanosecond fluorescence

lifetime experiments for NIR emissions were performed by using a time-correlated single-photon-counting (TCSPC) system on the single crystal samples on a Horiba Jobin Deltaflex fluorescence spectrometer. The doped MAPbBr$_3$ samples were excited at $\lambda = 485$ nm by using a DeltaDiode-485 as the excitation light source, and emitted photons were detected by means of a H10330B-75 photomultiplier tube (PMT) detector (with a high-pass single-edge filter, the edge wavelength of which was $\lambda = 830$ nm, inserted between the sample and detector). The fluorescence decay data were analyzed by using DAS-6 fluorescence decay analysis software with a global analysis program. The quality of the exponential fits was evaluated by $\chi^2 < 2.0$. XPS was measured by using a Thermal Fisher ESCALAB 250Xi surface analysis system. The measurements were conducted at room temperature and the analysis area was a circle with a diameter of 400 μm.

Conflict of interest

The authors declare no conflict of interest.

Keywords: bismuth · doping · luminescence · photochemistry · perovskite phases

[1] T. M. Brenner, D. A. Egger, L. Kronik, G. Hodes, D. Cahen, *Nat. Rev. Mater.* **2016**, *1*, 15007.

[2] G. Xing, N. Mathews, S. Sun, S. S. Lim, Y. M. Lam, M. Grätzel, S. Mhaisalkar, T. C. Sum, *Science* **2013**, *342*, 344–347.

[3] J. T. Tisdale, E. Muckley, M. Ahmadi, T. Smith, C. Seal, E. Lukosi, B. Hu, *Adv. Mater. Interfaces* **2018**, *5*, 1800476.

[4] Z. K. Tan, R. S. Moghaddam, M. L. Lai, P. Docampo, R. Higler, F. Deschler, M. Price, A. Sadhanala, L. M. Pazos, D. Credgington, F. Hanusch, T. Bein, H. J. Snaith, R. H. Friend, *Nat. Nanotechnol.* **2014**, *9*, 687–692.

[5] W. Nie, H. Tsai, R. Asadpour, J.-C. Blancon, A. J. Neukirch, G. Gupta, J. J. Crochet, M. Chhowalla, S. Tretiak, M. A. Alam, H.-L. Wang, A. D. Mohite, *Science* **2015**, *347*, 522–525.

[6] Q. Dong, Y. Fang, Y. Shao, P. Mulligan, J. Qiu, L. Cao, J. Huang, *Science* **2015**, *347*, 967–970.

[7] D. Shi, V. Adinolfi, R. Comin, M. Yuan, E. Alarousu, A. Buin, Y. Chen, S. Hoogland, A. Rothenberger, K. Katsiev, Y. Losovyj, X. Zhang, P. A. Dowben, O. F. Mohammed, E. H. Sargent, O. M. Bakr, *Science* **2015**, *347*, 519–522.

[8] T. Niu, J. Lu, R. Munir, J. Li, D. Barrit, X. Zhang, H. Hu, Z. Yang, A. Amassian, K. Zhao, S. Liu, *Adv. Mater.* **2018**, *30*, 1706576.

[9] C. La-o-vorakiat, T. Salim, J. Kadro, M. T. Khuc, R. Haselsberger, L. Cheng, H. Xia, G. G. Gurzadyan, H. Su, Y. M. Lam, R. A. Marcus, M. E. Michel-Beyerle, E. E. Chia, *Nat. Commun.* **2015**, *6*, 7903.

[10] W. Zhang, S. Pathak, N. Sakai, T. Stergiopoulos, P. K. Nayak, N. K. Noel, A. A. Haghighirad, V. M. Burlakov, D. W. Dequilettes, A. Sadhanala, W. Li, L. Wang, D. S. Ginger, R. H. Friend, H. J. Snaith, *Nat. Commun.* **2015**, *6*, 10030.

[11] S. D. Stranks, H. J. Snaith, *Nat. Nanotechnol.* **2015**, *10*, 391–402.

[12] R. Begum, M. R. Parida, A. L. Abdelhady, B. Murali, N. M. Alyami, G. H. Ahmed, M. N. Hedhili, O. M. Bakr, O. F. Mohammed, *J. Am. Chem. Soc.* **2017**, *139*, 731–737.

[13] A. H. Slavney, T. Hu, A. M. Lindenberg, H. I. Karunadasa, *J. Am. Chem. Soc.* **2016**, *138*, 2138–2141.

[14] Z. Zhang, L. Ren, H. Yan, S. Guo, S. Wang, M. Wang, K. Jin, *J. Phys. Chem. C* **2017**, *121*, 17436–17441.

[15] Q. Jiang, M. Chen, J. Li, M. Wang, X. Zeng, T. Besara, J. Lu, Y. Xin, X. Shan, B. Pan, C. Wang, S. Lin, T. Siegrist, Q. Xiao, Z. Yu, *ACS Nano* **2017**, *11*, 1073–1079.

[16] L. A. Frolova, D. V. Anokhin, K. L. Gerasimov, N. N. Dremova, P. A. Troshin, *J. Phys. Chem. Lett.* **2016**, *7*, 4353–4357.

[17] J. T.-W. Wang, Z. Wang, S. Pathak, W. Zhang, D. W. Dequilettes, F. Wisnivesky-Rocca-Rivarola, J. Huang, P. K. Nayak, J. B. Patel, H. Yusof, Y. Vaynzof, R. Zhu, I. Ramirez, J. Zhang, C. Ducati, C. Grovenor, M. B. Johnston, D. S. Ginger, R. J. Nicholas, H. J. Snaith, *Energy Environ. Sci.* **2016**, *9*, 2892–2901.

[18] X. Miao, T. Qiu, S. Zhang, H. Ma, Y. Hu, F. Bai, Z. Wu, *J. Mater. Chem. C* **2017**, *5*, 4931–4939.

[19] P. K. Nayak, M. Sendner, B. Wenger, Z. Wang, K. Sharma, A. J. Ramadan, R. Lovrincic, A. Pucci, P. K. Madhu, H. J. Snaith, *J. Am. Chem. Soc.* **2018**, *140*, 574–577.

[20] A. L. Abdelhady, M. I. Saidaminov, B. Murali, V. Adinolfi, O. Voznyy, K. Katsiev, E. Alarousu, R. Comin, I. Dursun, L. Sinatra, E. H. Sargent, O. F. Mohammed, O. M. Bakr, *J. Phys. Chem. Lett.* **2016**, *7*, 295–301.

[21] Y. Yamada, Y. Hoyano, R. Akashi, K. Oto, Y. Kanemitsu, *J. Phys. Chem. Lett.* **2017**, *8*, 5798–5803.

[22] C. Li, X. Lu, W. Ding, L. Feng, Y. Gao, Z. Guo, *Acta Crystallogr. Sect. B* **2008**, *64*, 702–707.

[23] W. Tress, N. Marinova, O. Inganäs, M. K. Nazeeruddin, S. M. Zakeeruddin, M. Graetzel, *Adv. Energy Mater.* **2015**, *5*, 1400812.

[24] T. Zhang, M. Yang, E. E. Benson, Z. Li, J. van de Lagemaat, J. M. Luther, Y. Yan, K. Zhu, Y. Zhao, *Chem. Commun.* **2015**, *51*, 7820–7823.

[25] Y. Liu, Z. Yang, D. Cui, X. Ren, J. Sun, X. Liu, J. Zhang, Q. Wei, H. Fan, F. Yu, X. Zhang, C. Zhao, S. F. Liu, *Adv. Mater.* **2015**, *27*, 5176–5183.

[26] Y. Zhang, Y. Liu, Y. Li, Z. Yang, S. Liu, *J. Mater. Chem. C* **2016**, *4*, 9172–9178.

[27] H. M. Liu, R. Nakamura, Y. Nakato, *J. Electrochem. Soc.* **2005**, *152*, G856–G861.

[28] J. Zhang, M. Shang, P. Wang, X. Huang, J. Xu, Z. Hu, Y. Zhu, L. Han, *ACS Energy Lett.* **2016**, *1*, 535–541.

[29] E. Mosconi, B. Merabet, D. Meggiolaro, A. Zaoui, F. D. Angelis, *J. Phys. Chem. C* **2018**, *122*, 14107–14112.

[30] Y. Hu, F. Bai, X. Liu, Q. Ji, X. Miao, T. Qiu, S. Zhang, *ACS Energy Lett.* **2017**, *2*, 2219–2227.

[31] P. Van Mieghem, *Rev. Mod. Phys.* **1992**, *64*, 755–793.

[32] V. Palankovski, G. Kaiblinger-Grujin, S. Selberherr, *Mater. Sci. Eng. B* **1999**, *66*, 46–49.

[33] Y. Kanemitsu, *J. Mater. Chem. C* **2017**, *5*, 3427–3437.

[34] X. Gong, Z. Yang, G. Walters, R. Comin, Z. Ning, E. Beauregard, V. Adinolfi, O. Voznyy, E. H. Sargent, *Nat. Photonics* **2016**, *10*, 253–257.

[35] T. Yamada, Y. Yamada, H. Nishimura, Y. Nakaike, A. Wakamiya, Y. Murata, Y. Kanemitsu, *Adv. Electron. Mater.* **2016**, *2*, 1500290.

[36] Y. Yuan, Q. Wang, Y. Shao, H. Lu, T. Li, A. Gruverman, J. Huang, *Adv. Energy Mater.* **2016**, *6*, 1501803.

[37] Y. Yuan, J. Huang, *Acc. Chem. Res.* **2016**, *49*, 286–293.

[38] S.-Y. Chung, I.-D. Kim, S.-J. L. Kang, *Nat. Mater.* **2004**, *3*, 774–778.

[39] S. Abe, K. Masumoto, K. Suto, *J. Cryst. Growth* **1997**, *181*, 367–373.

[40] H. T. Yi, X. Wu, X. Zhu, V. Podzorov, *Adv. Mater.* **2016**, *28*, 6509–6514.

[41] Y. Shao, Z. Xiao, C. Bi, Y. Yuan, J. Huang, *Nat. Commun.* **2014**, *5*, 5784.

[42] J. Xu, A. Buin, A. H. Ip, W. Li, O. Voznyy, R. Comin, M. Yuan, S. Jeon, Z. Ning, J. J. McDowell, P. Kanjanaboos, J. P. Sun, X. Lan, L. N. Quan, D. H. Kim, I. G. Hill, P. Maksymovych, E. H. Sargent, *Nat. Commun.* **2015**, *6*, 7081.

[43] S. Meloni, T. Moehl, W. Tress, M. Franckevicius, M. Saliba, Y. H. Lee, P. Gao, M. K. Nazeeruddin, S. M. Zakeeruddin, U. Rothlisberger, M. Graetzel, *Nat. Commun.* **2016**, *7*, 10334.

[44] W. Zhang, G. E. Eperon, H. J. Snaith, *Nat. Energy* **2016**, *1*, 16048.

[45] Y. Yuan, J. Chae, Y. Shao, Q. Wang, Z. Xiao, A. Centrone, J. Huang, *Adv. Energy Mater.* **2015**, *5*, 1500615.

[46] A. Poglitsch, D. Weber, *J. Chem. Phys.* **1987**, *87*, 6373–6378.

[47] V. I. Arkhipov, P. Heremans, E. V. Emelianova, H. Bässler, *Phys. Rev. B* **2005**, *71*, 045214.

[48] J. Choi, J. S. Han, K. Hong, S. Y. Kim, H. W. Jang, *Adv. Mater.* **2018**, *30*, 1704002.

[49] D. Bi, C. Yi, J. Luo, J. D. Décoppet, F. Zhang, S. M. Zakeeruddin, X. Li, A. Hagfeldt, M. Grätzel, *Nat. Energy* **2016**, *1*, 16142.

[50] J. Han, L. Li, M. Peng, B. Huang, F. Pan, F. Kang, L. Li, J. Wang, B. Lei, *Chem. Mater.* **2017**, *29*, 8412–8424.

[51] R. D. Shannon, *Acta Crystallogr.* **2015**, *32*, 751–767.